Korean J. Chem. Eng., 36(2), 226-235 (2019)
DOI: 10.1007/s11814-018-0190-x

pISSN: 0256-1115
eISSN: 1975-7220

Aminated cassava residue-based magnetic microspheres for Pb(II) adsorption from wastewater

Xinling Xie[*,], Jie Huang[*], Youquan Zhang[*,†], Zhangfa Tong[*], Anping Liao[***], Xingkui Guo[**,****], Zuzeng Qin[*,†], and Zhanhu Guo[**,†]**

*School of Chemistry and Chemical Engineering, Guangxi Key Laboratory of Petrochemical Resource Processing and Process Intensification Technology, Guangxi University, Nanning 530004, Guangxi, China
**Integrated Composites Laboratory (ICL), Department of Chemical and Biomolecular Engineering, University of Tennessee, Knoxville, Tennessee 37966, USA
***Key Laboratory of Chemical and Biological Transformation Process of Guangxi Higher Education Institutes, Guangxi University for Nationalities, Nanning 530006, Guangxi, China
****College of Chemical and Environmental Engineering, Shandong University of Science and Technology, Qingdao 266590, China

(*Received 20 July 2018 • accepted 14 November 2018*)

Abstract−Aminated cassava residue magnetic microspheres (ACRPM) were synthesized via an inverse emulsion method by using chemically modified cassava residue as a crude material, and acrylic acid (AA), acrylamide (AM), and methyl methacrylate (MMA) as monomers and a polyethylene glycol/methanol system (PEG/MeOH) as the porogen. Fourier-transform infrared spectroscopy (FT-IR), X-ray diffraction (XRD), scanning electron microscopy (SEM), transmission electron microscopy (TEM), N_2 adsorption-desorption and vibrating sample magnetometry (VSM) were used to characterize the ACRPM. The results indicated that amino groups were grafted to the cassava residue magnetic microspheres, and the Fe_3O_4 nanoparticles were encapsulated in the microspheres. After porogen was added, the particle size of the ACRPM decreased from 16.5 μm to 150 nm with a pore volume of 0.05510 m^3/g, and the specific surface area of the ACRPM increased from 3.02 to 12.34 m^2/g. The ACRPM were superparamagnetic, and the saturation magnetization was 9.8 emu/g. The maximum adsorption capacity of Pb(II) on the ACRPM was 390 mg/g. The ACRPM exhibited a large specific surface area and provided many adsorption sites for metal ion adsorption, which favored a high adsorption capacity. Additionally, the Pb(II) adsorption process was fitted to pseudo-second-order kinetic and Langmuir isothermal adsorption models. This suggests that the Pb(II) adsorption process was dominated by a chemical reaction process and that chemisorption was the rate-controlling step during the Pb(II) removal process. In addition, the adsorbent exhibited good stability after six consecutive reuses.

Keywords: Aminated Cassava Residue, Magnetic Microspheres, Inverse Emulsion, Polyethylene Glycol/Methanol System, Pb(II), Adsorption

INTRODUCTION

Although rapid industrial and economic development has brought enormous economic benefits, a series of forms of environmental pollution have also been caused, among which heavy metal pollution is one of the most biologically damaging [1]. Heavy metals can stress aquatic organisms in coastal ecosystems and concomitantly endanger human health [2]. Most heavy metals are nondegradable and toxic, which causes serious health hazards to humans. There are many routes of public exposure to lead, including lead in some pigments, food or old refrigerators [3], and lead poisoning leads to the deterioration of the nervous system and contributes to serious health issues [4]. Subsequently, heavy metal pollution has drawn global attention in recent years [5,6]. This great concern has led to a search for new and effective methods for the removal of heavy metal ions from food chains [7], and many methods have been developed to reduce heavy metal pollution, including adsorption [8], complexation, photodegradation [9], electrodialysis, and reverse osmosis [10]. Among these, adsorption is considered the most effective and feasible due to its cost effectiveness, easy operation, versatile nature, mild operating conditions and high efficiency [11]. Common adsorbents include humic acid [12], mesoporous materials such as SiO_2 [13], and polymeric adsorbents [14]. Among these, magnetic microspheres, a highly attractive adsorbent with magnetic character and a spherical particle shape, can electrostatically attract and remove metallic ions in wastewater [15]. Magnetic microspheres can also be easily separated from wastewater and reused [16].

In particular, magnetic polymer microspheres containing natural polymer adsorbents have the advantage of being low cost, nontoxic, renewable and biodegradable, and can be used as potential adsorbents in many water-treatment fields. These absorbents are usu-

†To whom correspondence should be addressed.
E-mail: zyq1968@163.com, qinzuzeng@gxu.edu.cn, zguo10@utk.edu

ally prepared by encapsulation [17], in situ polymerization [18], monomer polymerization [19], free radical polymerization [20], or inverse emulsion [21]. Among these, inverse emulsion is considered superior due to the high polymerization degree, good sphericity of the microspheres, and low reaction temperature [21]. Magnetic polymer microspheres have been reported with wide applications in recent years [22], including glycoprotein separation [23] and the adsorption of dansyl amino acids [24].

Cassava is widely used for starch production and fermentation products due to its high starch content [25]. With the increasing demand for starch- and the cassava-based ethanol production, the cassava processing industry has increased immensely, which has resulted in an increasing amount of related waste residue [26]. Generally, cassava residue is used as fodder, as fuel for heat production, and in anaerobic biogas fermentation [27]; however, the utilization ratio of cassava residue is still low. Cassava residue contains a large amount of cellulose and starch and has already exhibited great potential for reuse in many fields [28], e.g., as a crude material for the preparation of magnetic microspheres, which can be used to remove the heavy metals from wastewater [29].

Magnetic cassava residue microspheres are magnetic composite materials formed by inorganic magnetic particles, cassava residue, and polymer, which are believed to possess special dual functions of polymer materials and magnetic particles, such microspheres are a potential adsorbent for heavy metals [30]. However, the functional groups of these absorbents have low effectiveness. On the other hand, amino groups are believed to be highly electronegative and hence electrostatically attract metal ions [31]. Therefore, to solve the problem of the low effectiveness functional groups, in the previous studies [29], magnetic microspheres with a high content of functional groups have been prepared by subjecting cassava reside to graft copolymerization and modification with amino groups in the present study.

The adsorption capacity and adsorption rate strongly depend on the particle size and specific surface area of adsorbents. How to accurately build and prepare small, homogeneous and dispersed multifunctional nanoparticles is still a challenge [23]. To reduce the particle size and increase the specific surface area of magnetic microspheres [29], porogen was added during the preparation of the magnetic microspheres, and cassava residues were subjected to modification via grafting. The preparation of magnetic microspheres by adding porogen has rarely been studied.

We prepared novel amino-modified cassava residue magnetic microspheres (ACRPM) via an inverse emulsion method with chemically modified cassava residue as the raw material: acrylic acid (AA), acrylamide (AM), and methyl methacrylate (MMA) as the grafted monomers; and a polyethylene glycol/methanol system (PEG/MeOH) as the porogen. The resulting material was used to remove Pb(II) from aqueous solution. The adsorbents were characterized by FT-IR, X-ray diffraction (XRD), scanning electron microscopy (SEM), transmission electron microscopy (TEM), particle size analysis and vibrating sample magnetometry (VSM). Reaction conditions such as the adsorption temperature, the solution pH, the amount of porogen and the adsorption time were optimized in a batch adsorption experiment, and the adsorption isotherm and kinetic models were also investigated.

EXPERIMENTAL

1. Materials

Cassava residue was obtained from Guangxi Mingyang Biochemical Technology Co., Ltd. (Nanning, China). Sodium bicarbonate ($NaHCO_3$), ethylenediamine, lead nitrate ($PbNO_3$), sodium hydroxide (NaOH) and hydrochloric acid (HCl) were purchased from Guanghua Technology Co., Ltd. (Guangdong, China). Acetic acid, acetone and methanol were purchased from Kelong Chemical Reagent Co., Ltd. (Chengdu, China). Acrylamide (AM), liquid paraffin, and hydrogen nitrate (HNO_3) were obtained from Damao Chemical Reagent Co., Ltd. (Tianjin China). Ammonium peroxydisulfate (APS), Op-4, acrylic acid (AA), and polyethylene glycol (PEG) were obtained from Xilong Chemical Reagent Co., Ltd. (Shantou, China). N,N′-Methylenebisacrylamide (MBAA), sorbitan fatty acid ester (Span-80), and epichlorohydrin (ECH) were purchased from Macklin Reagent Co., Ltd. (Shanghai, China). All the chemicals used in this study were analytical grade and used without further purification.

2. Pretreatment of Cassava Residue

Cassava residue (CR) was crushed and screened through a 50-mesh screen, Then 100 g CR was pretreated with sodium hydroxide (4 wt%) at 353 K for 2 h, and further treated with 27 g sodium hydroxide, 18.8 g sodium bicarbonate, 75 mL acetic acid and 1,000 mL deionized water at 353 K for 6 h to obtain pretreated cassava residue (PCR). The PCR was again immersed in a mixture of sodium hydroxide solution (5 wt%), 200 mL epichlorohydrin (ECH) and 400 mL absolute ethanol (cosolvent) at 333 K for 3 h with stirring at 600 r/min. Subsequently, the treated residue was dispersed in a solution of 80 g sodium hydroxide, 900 mL deionized water and 120 mL ethylenediamine at 353 K for 6 h, resulting in epoxidated and aminated cassava residue (ACR), which was washed with deionized water until reaching neutral pH. Finally, the ACR was ground to powder after drying in an oven at 50 °C for 24 h.

3. Preparation of ACRPM

The ACRPM were prepared as follows: 0.8 g ACR, 0.817 g NaOH and 6 mL deionized water were mixed in a beaker and stirred in an ice-water bath using a magnetic stirrer with a dropwise side addition of 3 mL MMA (1 wt%). After the solution was cooled to room temperature, a mixture of 3.75 mL AA, 1.0 g AM, and 0.018 g MBAA was added to the above solution. After 10 min stirring, 0.0302 g Na_2SO_3, 0.0547 g APS and 2.5 g porogen (polyethylene glycol/methanol) were added as the evocating agent to the above mixture, and 0.4 g nano-Fe_3O_4 (20-30 nm) was immersed in a beaker and stirred for 30 s. Then, 12.375 g Span-80 and 2.625 g OP-4 (emulsifiers) were dissolved in 15 mL liquid paraffin in three different flasks and stirred at 300-400 rpm and 283 K. Mixing of the oil phase was followed by immediate addition of the water phase, and the reaction was maintained at 283.15 K. After 30 min, the temperature was raised to 323 K, and stirring was continued for 3 h. All the polymerization processes were conducted under a nitrogen atmosphere with continuous stirring. Finally, the microspheres were washed with ethanol and acetone and dried at 323 K. Aminated cassava residue magnetic microspheres were prepared by the same procedure as the ACRPM but without the addition of porogen and are identified as ACRM.

4. Characterization of the ACRM and ACRPM

The surface morphology of the ACRM and ACRPM was analyzed using scanning electron microscopy (SEM, S-3400 N, Hitachi, Japan) and transmission electron microscopy (TEM, Tecnai G2 F30 S-Twin, FEI, USA). Elemental content was analyzed on an SEM-EDX spectrometer using a filament voltage of 129 eV. The magnetic intensity of the ACRPM was analyzed by using a vibrating sample magnetometer (VSM, 7410, LakeShore, USA). Thermogravimetric and differential thermal analyses of the ACRM and the ACRPM were performed by differential scanning calorimeter (TG-DSC, RVC2-18, Netzsch, Germany). The surface groups of the CR, ACR and ACRPM were analyzed by Fourier transform infrared spectroscopy (FTIR, Nicolet FTIR IS10, USA) in the wavenumber range of 4,000 to 400 cm^{-1}, and the textural properties were characterized by N_2 adsorption-desorption (BET, Gemini VII 2390, Micromeritics, USA). The crystal structure of the CR, PCR and ACR was analyzed on a Rigaku X-ray diffractometer (XRD, Smart Lab diffractometer, Japan).

5. Pb(II) Adsorption on ACRPM

Adsorption kinetic experiments were performed at 303 K as follows: 0.1 g ACRPM and 100 mL 500 mg/L Pb(II) solution were placed in a beaker, the pH of the mixture was adjusted to 5.5, and the beaker was shaken at 150 rpm. Samples were taken at different time intervals and diluted to measure the concentration by using a UV-Vis spectrophotometer (UV, TU-1900, Beijing Purkinje General Instrument Co., Ltd., China) at wavelengths of 621 nm and 572 nm.

The adsorption capacity of magnetic microspheres for heavy metals was calculated by using Eq. (1).

$$Q = \frac{V(C_0 - C)}{m} \quad (1)$$

where Q is the adsorption capacity (mg/g); C_0 and C are the metal ion concentration before and after adsorption (mg/mL), respectively; m is the weight of the magnetic microspheres (g); and V is the volume of the solution (mL).

6. ACRPM Desorption Experiments

The regeneration of adsorbents is an important aspect of adsorption studies. To determine the reusability of the ACRPM, the adsorption-desorption process was repeated six times. Adsorbent-loaded Pb(II) was added to a 0.1 mol/L HNO_3 (L) solution and stirred at 25 °C for 2 h to desorb the metal ions followed by rinsing with deionized water until reaching neutral pH; the wastewater produced during the soaking process could be used as a solution to adjust the pH. The adsorption capacity in each cycle was measured.

RESULTS AND DISCUSSION

1. Adsorbent Characterization

Fig. 1(A) shows the FTIR spectra of the CR, ACR, and ACRPM.

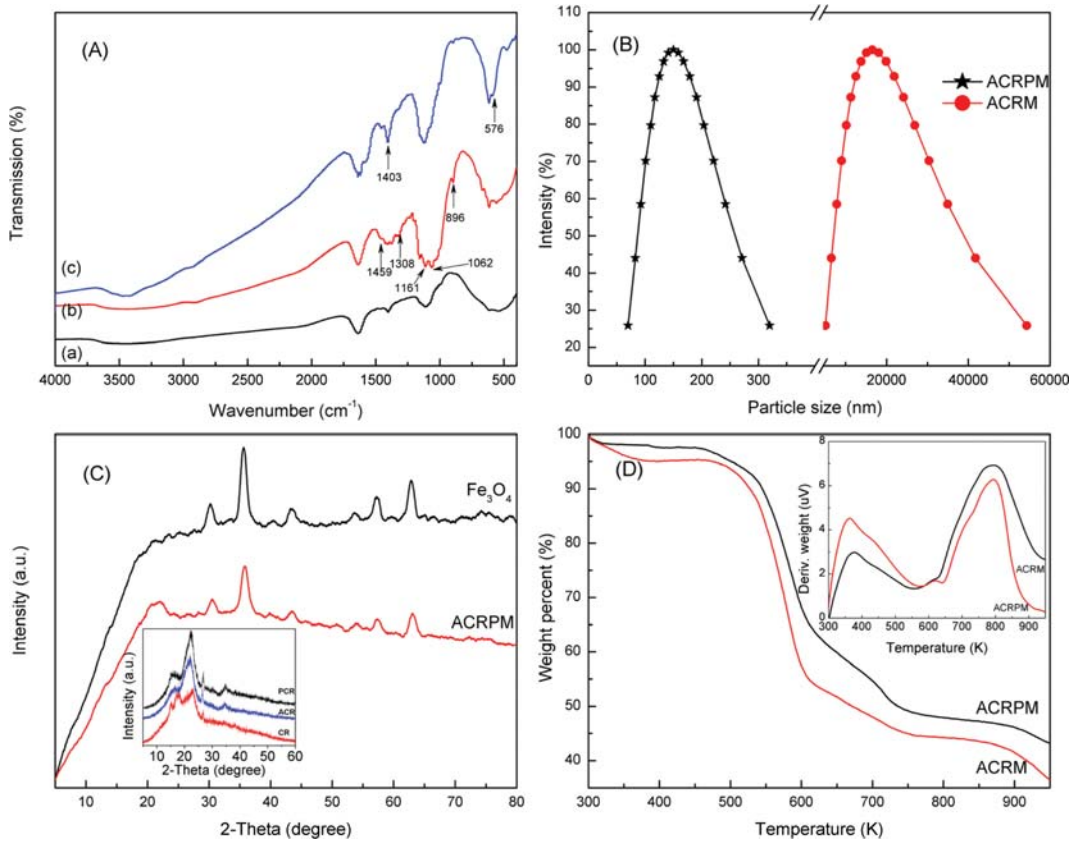

Fig. 1. (A) FT-IR spectra of (a) CR, (b) ACR, and (c) ACRPM; (B) The particle size distribution of the ACRM and ACRPM; (C) XRD patterns of ACRPM and Fe_3O_4, and the inset was XRD patterns of the CR, PCR, and ACR; (D) TGA analysis of the ACRM and the ACRPM, and the inset was DTA analysis of the ACRM and the ACRPM.

In the spectrum of ACR, the absorption peaks at 1,161.23, 895.59, and 1,062.11 cm^{-1} were assigned to the epoxy group stretching vibration [32], and the peaks at 1,307.93 and 1,458.59 cm^{-1} were assigned to the C-N stretching vibration of ethylenediamine [33], indicating that epichlorohydrin and ethylenediamine were successfully grafted onto the CR. The absorption peak of the ACRPM at 575.85 cm^{-1} was the Fe-O stretching vibration of Fe_3O_4, indicating the successful coating of Fe_3O_4 onto the aminated cassava residue microspheres. A new absorption peak was found at 1,403.06 cm^{-1} for the C-N stretching vibration of amine [18], which supported the existence of amino groups on the ACRPM adsorbent. The above results indicated that the amino group of ACR was grafted to ACRPM and that the ACRPM was wrapped with Fe_3O_4. However, the peak at 1,458.59 cm^{-1} disappeared in the ACRPM, indicating that the structure of the ACRPM changed during the modification process.

Fig. 1(B) shows the particle size distribution of the ACRM and ACRPM. The average particle size of the ACRM and the ACRPM was 16.5 μm and 150 nm, respectively. Compared with the ACRM (particle size of 16.5 μm) and crosslinked starch microsphere adsorbents reported in the literature (particle size of 9.253 μm) [34], the particle size of the ACRPM, 150 nm, was significantly reduced, suggesting that the pore size, particle size and specific surface area of the magnetic microspheres were greatly affected by the addition of the porogen. The addition of the pore-forming agent (PEG/MeOH) not only decreased the droplet size in the emulsion, but also decreased the viscosity of the magnetic microspheres due to the acrylic polymer and ACR starch.

Fig. 1(C) shows the XRD patterns of Fe_3O_4 and the ACRPM. The diffraction peaks located at 30.0°, 35.6°, 43.3°, 53.6°, 57.2° and 62.9° were due to the (220), (311), (400), (422), (511) and (440) planes of the Fe_3O_4 [35], indicating the successful incorporation of Fe_3O_4 into the ACRPM. XRD patterns of the CR, PCR, and ACR are shown in the inset of Fig. 1(C). The diffraction patterns of the CR at 2θ=17.8° and 22.8° were the characteristic peaks of cellulose I; however, the intensity of the peaks was low due to the high amount of lignin and hemicellulose, which contributed to the amorphization of lignocellulose in cassava residue. The diffraction peaks of cellulose I in the PCR at 2θ=16.7° and 22.4° [36] were due to the removal of lignin, hemicellulose, and other impurities, and led to the increased crystallinity and peak strength of the ACR and the PCR. Furthermore, compared with the PCR, the intensity of all the peaks of the ACR was decreased, suggesting that the chemical modification resulted in the reduction of hydrogen bond activity in the cellulose chains. These results further indicated the successful chemical modification of the PCR by ethylenediamine grafting.

Fig. 1(D) shows the TGA/DTA results for the samples. In Fig. 1(D), 58.2% and 65.2% weight losses were found in the ACRM and ACRPM, respectively, indicating that the ACRPM exhibited higher thermal stability than the ACRM, which was attributed to the formation of a stable mesoporous medium via the addition of porogen. The first weight loss of the ACRM and ACRPM between 303 and 373 K was due to water evaporation, and the second weight loss of the ACRM was found at 493-733 K, which was caused by the decomposition of the cellulose and the starch in the cassava residue. The same weight loss process in the ACRPM was attributed to the decomposition of the polymer and the monomer copolymer on the microspheres. The inset of Fig. 1(D) shows that in the ACRM and ACRPM, the first endothermic melting peak appeared at approximately 363-373 K and the second appeared at 773-783 K. These results were consistent with the particle size distribution results.

Fig. 2(a)-(e) shows SEM images of the magnetic microspheres and the effects of porogen addition on the microspheres. As shown in Fig. 2(a), the ACRM comprised magnetic microspheres that exhibited a smooth particle surface and a good sphericity with an average particle size of approximately 10 μm. From Fig. 2(b)-2(e), the magnetic microsphere structure changed considerably by varying the porogen amount. Fig. 2((b) and (c)) shows that the ACRPM aggregated into cluster at porogen amounts of 1.5 and 2.0 g. Fig. 2(c) shows the uneven particle sizes of ACRPM with slight agglomeration. However, the magnetic microspheres in Fig. 2(d) were well dispersed, exhibiting a spherical shape and a rather uniform particle size when 2.5 g porogen was added; therefore, the optimal porogen amount for the optimal microsphere particle size distribution

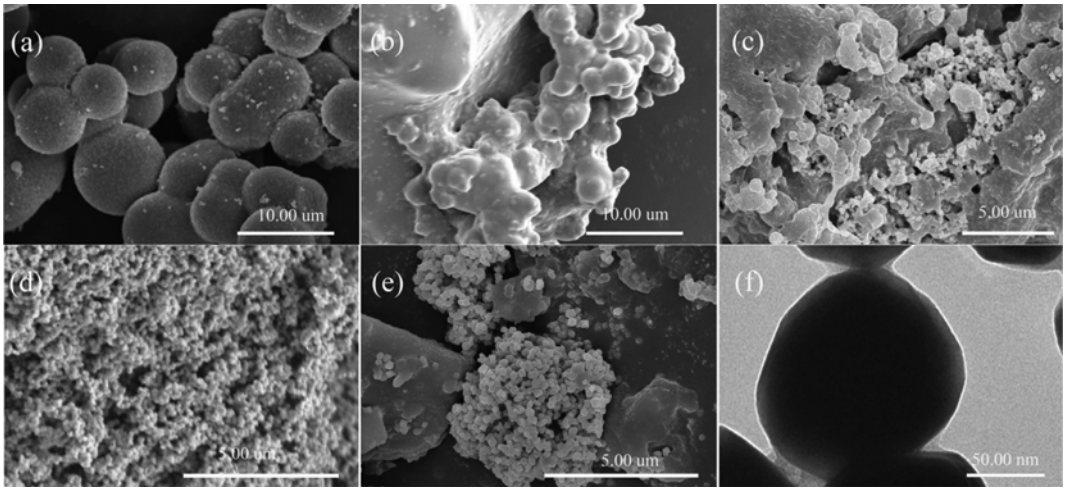

Fig. 2. SEM images of the ACRM (a) and the ACRPM using variable amount of porogen (PEG/MeOH=2 : 1, W : W)1.5 g (b), 2.0 g (c), 2.5 g (d), 3.0 g (e), and TEM image of the ACRPM (f).

was found to be 2.5 g (0.26 g/mL). The TEM image of the ACRPM in Fig. 2(f) shows a thin layer coated on the surface of the magnetic microspheres, which is attributed to the hydrophobicity of the MAA. The SEM and TEM images indicated that the addition of porogen (PEG/MeOH) decreased the droplet size in the emulsion and decreased the viscosity of the prepared magnetic microspheres; this change came from the acrylic acid and the starch of the ACR. These results are consistent with the particle size distribution results (Fig. 1(B)).

Fig. S1 shows the EDAX (energy dispersive X-ray analysis) of the ACRPM after adsorption of Pb(II) for the first time. After adsorption, Pb element peaks appeared in the ACRPM, indicating the adsorbed species. This suggested that the ACRPM had already adsorbed the Pb(II). Furthermore, the N peak in the microspheres indicated that the microspheres contained nitrogen-containing substances; the N came from amino groups grafted onto the ACR, which was consistent with the results of XRD and FT-IR analysis (Fig. 1).

Fig. 3 shows the magnetic hysteresis loop of ACRPM. The successful preparation of ACRPM was confirmed by the zero values of the remanence and coercivity of magnetization curves; i.e., no hysteresis was found. This indicated that the ACRPM have superparamagnetic behavior [30]. The saturation magnetization of the ACRPM was 9.8 emu/g. Therefore, the ACRPM could be easily and rapidly separated after adsorbing Pb(II) by applying an external magnetic field, as shown in the inset of Fig. 3.

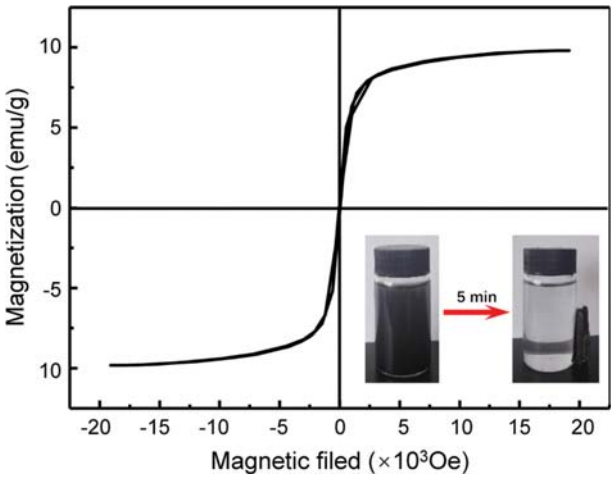

Fig. 3. Magnetization curves of the ACRPM, and the inset is the ACRPM separated from the Pb(II) solution in magnetic field.

The specific surface area and porosity analysis results for the ACRM and ACRPM are summarized in Table S1. The addition of the porogen led to an increase in specific surface area from 3.02 to 12.34 m^2/g, an increase in pore volume from 0.012 to 0.055 m^3/g and a reduction in pore size from 26.65 to 17.85 nm for the magnetic microspheres. Compared with crosslinked starch microsphere adsorbents reported in the literature (specific surface area 0.6484 m^2/g, pore volume 0.0032 cm^3/g, average particle size 9.253 μm) [37], the specific surface area and pore volume of the ACRPM were increased, and the pore size was decreased. Therefore, the ACRPM were good carriers and could adsorb more functional matter, which made them more favorable for the adsorption of Pb(II) in this study. The increased specific surface area and decreased pore size were attributed to the incorporation of the porogen species in the ACRPM molecules, which led to the separation of small agglomerates and exposed more surface sites for metal ion adsorption. From Fig. S2, the pore size for the ACRM and ACRPM was 26.65 nm and 17.85 nm, respectively, which confirmed that the pore size was mostly in the mesoporous range; furthermore, the ACRM and ACRPM exhibited highly ordered pore structure, a single pore size distribution, and good stability, which benefited the adsorption of Pb(II).

2. Effects of Adsorption Conditions

The effects of the contact time, the solution pH, the adsorption temperature and the amount of porogen on the adsorption capacity of the ACRPM for Pb(II) were studied. The results are shown in Fig. 4.

The solution pH is an important controlling factor during the adsorption process. Fig. 4(a) shows the influence of solution pH on the Pb(II) adsorption efficiency on the ACRPM. The Pb(II) adsorption capacity of the ACRPM increased from 30 to 388 mg/g

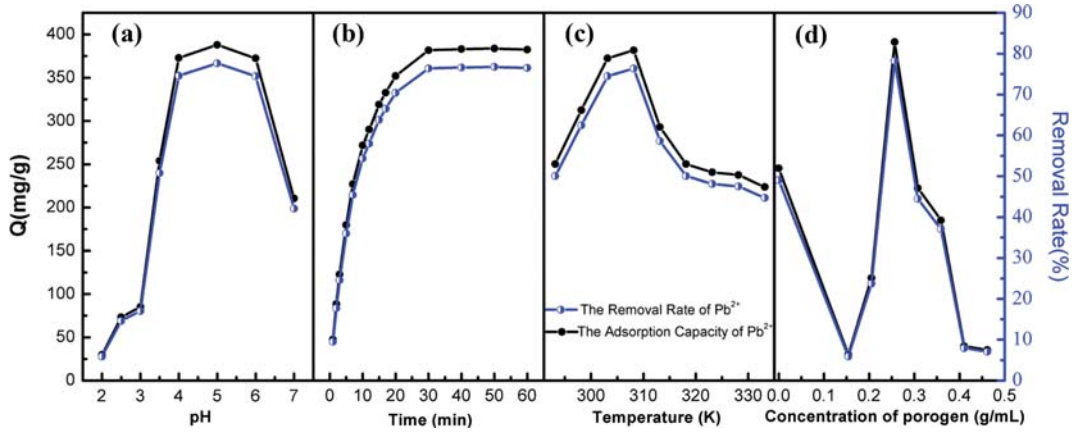

Fig. 4. Effects of the solution pH (a) (30 min, 308.15 K, porogen concentration 0.26 g/mL), the contact time (b) (pH=5, 308.15 K, porogen concentration 0.26 g/mL), the adsorbent temperature (c) (pH=5, 30 min, porogen concentration 0.2 g/mL), and the porogen (PEG/MeOH) amount (d) (pH=5, 30 min, 308.15 K) on the adsorption capacity of the Pb(II) on the ACRPM.

with increasing solution pH from 2.0 to 5.0 and then decreased to 244 mg/g when the solution pH was increased from 5.0 to 7.0, which was attributed to changes in the surface chemistry state of the adsorbent upon changing H^+ ion concentration [38]. At low pH, the high concentration of H^+ ions underwent competitive adsorption with the metal cations in solution for the adsorbent active sites, i.e., sites that could be utilized in an adsorption process, resulting in a lower adsorption value. In contrast, with increasing pH, the amount of H^+ ions decreased, which favored contact between the Pb(II) ions and the adsorbent active sites, resulting in a higher adsorption capacity. Another factor responsible for the higher adsorption capacities at higher pH values could be that the increase in negative charges on the adsorbent surface caused electrostatic attraction between Pb(II) ions and adsorbent sites with increasing pH, leading to a higher adsorption capacity. However, beyond pH 5.0, the precipitation of heavy metal ions led to a decrease in the adsorption capacity. The maximum capacity of 388 mg/g was obtained at pH 5.0.

To establish the adsorption equilibration time for the maximum adsorption capacity, the adsorption capacity of the ACRPM for Pb(II) was measured with respect to the adsorption contact time. The results are shown in Fig. 4(b). Fig. 4(b) shows that the adsorption capacity of the ACRPM increased rapidly during the first 10 min and then gradually decreased with increasing adsorption contact time, reaching an adsorption equilibrium of 383 mg/g at 30 min. At the start of the process, there were enough adsorption sites on the ACRPM surface available for metal ion adsorption, leading to a fast adsorption rate in the first 10 min. Upon further increasing the adsorption contact time, the corresponding number of active sites decreased, until the process reached adsorption equilibrium. The adsorption capacity of 383 mg/g was much higher and the adsorption equilibrium time of 30 min was much lower than the corresponding values reported in previous works [3,39]. Therefore, an adsorption equilibrium of 30 min was selected for subsequent experiments.

Fig. 4(c) shows the effects of adsorption temperature on the adsorption capacity of ACRPM for Pb(II). Fig. 4(c) shows that the adsorption capacity increased sharply from 250 to 382 mg/g upon increasing the temperature from 293 to 308 K, and slowly decreased from 382 to 224 mg/g upon further increasing the temperature from 308 to 333 K. These results might have occurred because the initial increased adsorption temperature led to an increase in the Brownian movement of Pb(II), increasing the effective collisions between the adsorbent and the metal ions. Further increases in adsorption temperature could cause the desorption of metal species by weakening the electrostatic attraction between the ACRPM and the Pb(II), leading to a decrease in adsorption capacity. The maximum Pb(II) adsorption capacity (382 mg/g) of the ACRPM was found at a relatively lower temperature of 308 K, indicating that the designed modified cassava residue magnetic microsphere-based adsorbent was more effective than traditional adsorbents [15,40]. Furthermore, a higher adsorption capacity and rate at a lower operating temperature could be of great importance for industrial applications, and the designed adsorbent exhibited the potential for heavy metal removal from wastewater and other industrial effluents.

As shown in Fig. 2, the presence and the amount of porogen could greatly alter the morphology of the ACRPM, which could directly affect the adsorption capacity as well. Fig. 4(d) shows the influence of the porogen amount on the adsorption capacity of the ACRPM for Pb(II). The adsorption capacity of the ACRM without porogen for Pb(II) was 245 mg/g. A sharp decrease in the adsorption capacity from 245 to 29 mg/g with increasing porogen concentration might have occurred because the initial increase in porogen concentration led to the aggregation of ACRPM into a cluster (as shown in Fig. 2(b)). Subsequently, the adsorption capacity of the ACRM sharply increased with increasing porogen concentration, and the maximum Pb(II) adsorption capacity of 391 mg/g for the ACRPM was found at a porogen concentration of approximately 0.26 g/mL. Further increasing the porogen concentration led to a decrease in the adsorption capacity of Pb(II). Upon increasing the adsorbent concentration (at values less than 0.26 g/mL), the sharp increase in adsorption capacity was due to the incorporation of the porogen, which led to a large fold increase in the specific surface area of the microspheres (as shown Fig. S2), increasing the number of contact sites between the adsorbent active sites and the metal ions and causing a higher adsorption capacity. Further increasing the porogen amount (beyond 0.26 g/mL) led to a corresponding decrease in the concentrations of the monomer and the crosslinking agent, causing a decrease in crosslinking degree, poor stability and a collapsible hole structure in the microspheres.

Table 1. Comparison of Pb(II) adsorption capacity on ACRPM with that on other adsorbents

Adsorbent	Adsorption conditions			Pb(II) adsorption capacity (mg/g)	Ref.
	Adsorption time (min)	pH	Temperature (K)		
Chemically modified cellulose	60	6	298.15	194	[41]
Porous starch xanthate	20	-	303.15	109.1	[42]
Porous starch citrate	60			57.6	
Oxidized starch nanoparticles	120	-	298.15	40.52	[43]
Novel melamine-modified metal-organic frameworks	120	6	313.15	205	[44]
Magnetic anaerobic granulated sludge/chitosan	-	6	298.15	97.97	[45]
Amino-functionalized magnetic mesoporous microspheres	120	6	Room temperature	289.7	[46]
Magnetic chitosan nanoparticles	720	6	296-300	79.24	[47]
ACRPM	30	5	308.15	390	This study

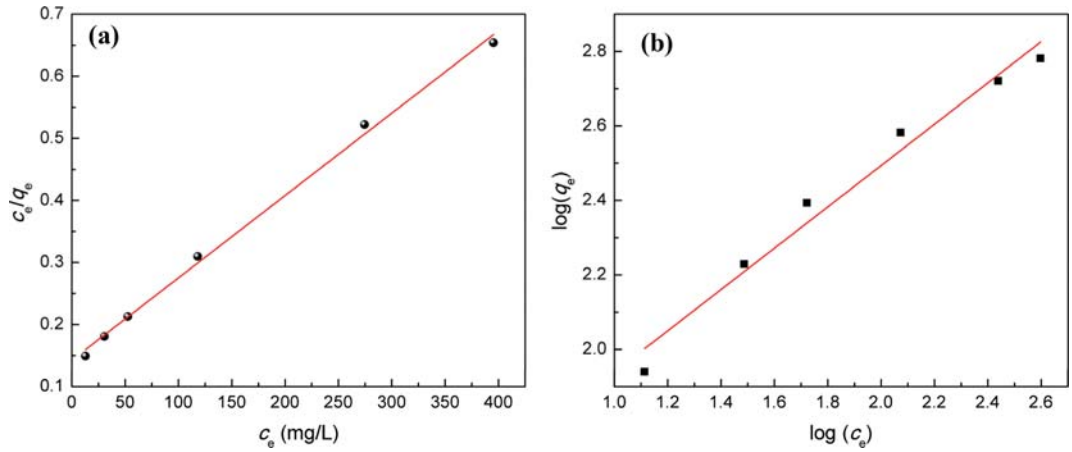

Fig. 5. Linear fitting of the adsorption data by using (a) the Langmuir isotherms model and (b) the Freundlich isotherms models of the Pb(II) ion adsorption on the ACRPM.

These results would also lead to decreases in the specific surface area and the amount of the adsorption sites and even a loss of sphericity in the resulting microspheres, which would ultimately decrease the adsorption capacity. These results were consistent with the SEM results (Fig. 2).

A comparison of the maximum adsorption capacities of Pb(II) on different adsorbents is summarized in Table 1. The maximum Pb(II) adsorption capacity of 390 mg/g for ACRPM was obtained within an adsorption equilibration time of 30 min in this study, which is higher than those in previous works. This shows that ACRPM have a good Pb(II) adsorption capacity compared with those of other adsorbents. This is probably because ACRPM have a larger specific surface area and a smaller particle size, which can enrich the contact between metal ions and amino groups in the channel. This confirms that ACRPM are a promising adsorption material for the removal of heavy metal ions from aqueous solutions.

3. Adsorption Isotherm Studies

To determine the adsorption efficiency of the ACRPM adsorbent for Pb(II) adsorption, adsorption isotherm experiments were carried out with initial Pb(II) concentrations from 10 to 500 mg/L. Two well-known models, the Langmuir and Freundlich isotherms [48], were used to describe the adsorption behavior and illustrate the type of adsorbent surface blinding mechanism [12].

The obtained experimental data were analyzed by the Langmuir and Freundlich equations following Eqs. (2) and (3), respectively [42]:

$$\frac{C_e}{q_e} = \frac{C_e}{q_m} + \frac{1}{q_m K_L} \quad (2)$$

$$\log(q_e) = \log(K_F) + \frac{\log(C_e)}{n} \quad (3)$$

where C_e (mg/L) is the concentration of metal ions at equilibrium adsorption, q_e (mg/g) is the equilibrium adsorption capacity, q_m (mg/g) is the saturated adsorption amount of the microspheres, K_L (L/mg) is the equilibrium constant of the Langmuir isotherm model, K_F is the relative constant of the Freundlich isotherm model, and the dimensionless exponent "n" is the adsorption intensity of the magnetic microspheres.

Table 2. Parameters of the Langmuir and Freundlich models for Pb(II) adsorption on ACRPM

Model	K_L (10^{-3} L/mg)	q_m (mg/g)	K_F	n	R^2
Langmuir	9.3	752	-	-	0.9962
Freundlich	-	-	24.22	1.80	0.9716

According to the Langmuir equation, the plot of C_e/q_e vs. c_e gives a straight line, and K_L and q_m can be calculated from the intercept and slope of the straight line, respectively. According to the Freundlich equation, the plot of log q_e verse log C_e gives a straight line, and K_F and n can be calculated from the intercept and slope of the straight line, respectively. The experimental results are shown in Fig. 5, and the fitting data obtained by using Eqs. (2) and (3) and the correlation coefficients for these two models are summarized in Table 2. Table 2 shows that the correlation coefficient of the Freundlich model was low (R^2=0.9716, which was less than 0.99). The correlation coefficient R^2 of 0.9962 for the Langmuir model confirmed good agreement between the theoretical model and the experimental data, which implies that the adsorption process can be better described by the Langmuir model than the Freundlich model. The adsorption of Pb(II) on ACRPM is characterized by monomolecular adsorption and the homogeneous distribution of active groups on the adsorbent surface. This suggests that the adsorption process of Pb(II) on the ACRPM was not a purely physical adsorption process and that there were chemical interactions between the adsorbent and the metal ions in solution [49]. The functional groups, -NH_2 and -OH, in the adsorbent played an important role in the adsorption process via electronically interacting with the charged metal ions in solution [50].

4. Adsorption Kinetics Studies

Adsorption kinetic models are usually used to study the change in adsorption capacity with respect to contact time (Fig. 4(b)) [51]. The adsorption process can be described by different adsorption mechanisms, such as mass transfer, chemical reaction and particle diffusion. To determine the adsorption behavior of Pb(II) on the ACRPM adsorbent, adsorption kinetic experiments were carried

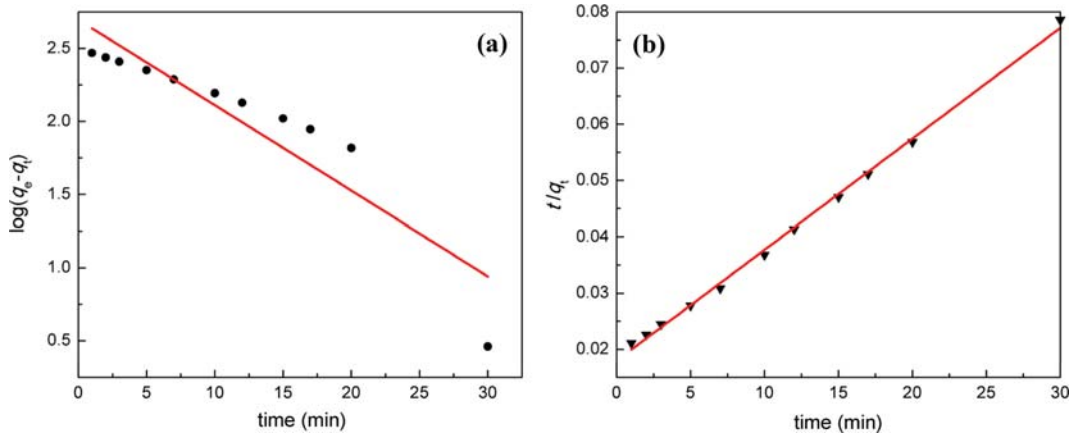

Fig. 6. Linear fitting of the adsorption data by using (a) the pseudo-first-order kinetic model, and (b) the pseudo-second-order kinetic model of the Pb(II) ion adsorption on the ACRPM adsorbent.

out. Two kinetic models were applied to evaluate the rate and parameters of adsorption of Pb(II) on the ACRPM adsorbent: the pseudo-first-order kinetic model (using Eq. (4)) and pseudo-second-order kinetic model (using Eq. (5)) [51]:

$$\log(q_e - q_t) = \log q_e - \frac{k_1}{2.303}t \quad (4)$$

$$\frac{t}{q_t} = \frac{1}{k_2 q_e^2} + \frac{1}{q_e}t \quad (5)$$

where k_1 (min^{-1}) is the pseudo-first-order rate constant, k_2 ($g \cdot mg^{-1} min^{-1}$) is the pseudo-second-order rate constant, q_e (mg/g) is the equilibrium adsorption capacity, and q_t (mg/g) is the adsorption capacity at time t.

The pseudo-first-order kinetic model is mainly based on the number of active adsorption sites, which directly determines the adsorption capacity, while the pseudo-second-order kinetic model is directly proportional to the amount of active adsorption sites [51]. The slope and intercept of the straight line of $\log(q_e - q_t)$ versus t can be used to calculate the pseudo-first-order rate constant (k_1) and q_e ($_{cal}$), as shown in Fig. 6(a). The slope and intercept of the straight line of t/q_t versus t can be used to calculate the pseudo-second-order rate constant (k_2) and q_e ($_{cal}$), as shown in Fig. 6(b). All the fitting parameters and correlation coefficients for these two models are summarized in Table 3. Table 3 shows that the correlation coefficient of the pseudo-first-order kinetic model (R^2=0.825) is less than 0.99, implying that the pseudo-first-order kinetic model does not provide a satisfactory fit for the Pb(II) adsorption process of the ACRPM adsorbent. The correlation coefficient R^2 value of 0.9976 for the pseudo-second-order kinetic model demonstrates that the adsorption of Pb(II) on the ACRPM adsorbent obeys the pseudo-second-order kinetic model, the adsorption process for Pb(II) on the ACRPM is dominated by the chemical reaction process and chemisorption is the rate-controlling step rather than mass transfer in solution. These results are consistent with the Langmuir isotherm model. Similar results were also obtained for the adsorption of Pb(II) ions from aqueous solution using amino-modified magnetic mesoporous microsphere adsorbents [46]. The rate constant (k_1) of Pb(II) on the ACRPM was 0.216 min^{-1}, which was higher than those reported in the literature. For example, compared with crosslinked starch microspheres (k_2=0.107×10^{-4} min^{-1}) and amino-modified magnetic mesoporous microspheres (k_2=0.004 min^{-1}) used as absorbents [46], the designed ACRPM adsorbents prepared by amino modification and graft copolymerization had more functional groups, provided more active adsorption sites and thus were capable of anchoring more heavy metal ions. Furthermore, the ACRPM, which had a larger specific surface area and a smaller particle size due to the addition of a porogen, provided more contact between the heavy metal ions and the adsorbent, resulting

Table 3. Kinetic model parameters for Pb(II) adsorption on ACRPM

Kinetic model	k_1 (min^{-1})	k_2 (g/mg·min)	$q_{e,cal}$ (mg/g)	R^2
Pseudo-first-order	0.135	-	497	0.825
Pseudo-second-order	-	2.16×10^{-4}	508	0.9976

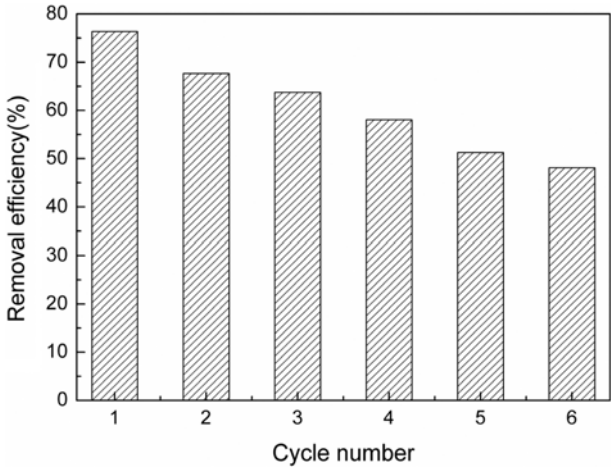

Fig. 7. The reusability of the ACRPM for the Pb(II) ions removal in six adsorption-desorption cycles (at pH=5.5, 303.15 K, the solution with initial concentration of the Pb(II) 500 mg/L, and the desorption and regeneration of the ACRPM 0.1 g).

in a faster adsorption rate. Therefore, these two characteristics of the ACRPM adsorbent greatly improved the adsorption capacity.

5. Reusability of ACRPM

The regeneration of adsorbents is important for industrial operation and can greatly decrease process costs and save time. The ACRPM was regenerated by immersing the material in 500 mL of 0.1 mol/L HNO_3 solution for 120 min, and the adsorption capacity of the regenerated ACRPM was tested under the same experimental conditions as that of fresh ACRPM. The results for this set of experiments are listed in Fig. 7. The removal efficiency of the regenerated adsorbent for Pb(II) remained active though six cycles of adsorption. The decrease in adsorption capacity may be attributed to the desorption of metal ions via ion exchange, where H^+ occupies the adsorption sites on the adsorbent.

CONCLUSIONS

We synthesized ACRPM via an inverse emulsion method, with polyethylene glycol/methanol as a porogen. The textural characterization results showed that amino functional groups were successfully grafted onto the CR, and the pore size of the magnetic microspheres was effectively reduced by adding PEG/MeOH as a porogen. At 308 K and a weak acidic environment, the ACRPM exhibited a high adsorption capacity of 390 mg/g for Pb(II) within 30 min. Adsorption isotherm analysis revealed that the Pb(II) adsorbed on the ACRPM fit the Langmuir model, indicating that physicochemical and multilayer adsorption occurred. Furthermore, the adsorption behavior of Pb(II) on the ACRPM was more consistent with a pseudo-second-order kinetic model, indicating that the adsorption capacity of the magnetic microspheres was related to the number of active sites, which is the controlling factor in adsorption capacity. Overall, the high adsorption capacity of the ACRPM throughout multiple cycles demonstrated good stability and reusability for Pb(II) removal from different industrial effluents in aqueous media.

ACKNOWLEDGEMENTS

This work was supported by the National Natural Science Foundation of China (No. 21766001), the China Scholarship Council (No. 201608455016), Guangxi Natural Science Foundation of China (No. 2015GXNSFAA139021), the Dean Project of Guangxi Key Laboratory of Petrochemical Resource Processing and Process Intensification Technology (No. 2016Z007), Guangxi Science and Technology Research Project (No. KY2015ZD005), and the Scientific Research Foundation of Guangxi University (No. XTZ140787).

SUPPORTING INFORMATION

Additional information as noted in the text. This information is available via the Internet at http://www.springer.com/chemistry/journal/11814.

REFERENCES

1. E. Da'na, *Micropor. Mesopor. Mater.*, **247**, 145 (2017).
2. G. Tepanosyan, L. Sahakyan, O. Belyaeva, N. Maghakyan and A. Saghatelyan, *Chemosphere*, **184**, 1230 (2017).
3. J. Ma, Y. Liu, O. Ali, Y. Wei, S. Zhang, Y. Zhang, T. Cai, C. Liu and S. Luo, *J. Hazard. Mater.*, **344**, 1034 (2018).
4. T. A. Kurniawan, G. Y. Chan, W. H. Lo and S. Babel, *Sci. Total Environ.*, **366**, 409 (2006).
5. Y. Ma, L. Lv, Y. Guo, Y. Fu, Q. Shao, T. Wu, S. Guo, K. Sun, X. Guo, E. K. Wujcik and Z. Guo, *Poly*, **128**, 12 (2017).
6. J. Huang, Y. Cao, Q. Shao, X. Peng and Z. Guo, *Ind. Eng. Chem. Res.*, **56**, 10689 (2017).
7. U. K. Garg, M. P. Kaur, V. K. Garg and D. Sud, *J. Hazard. Mater.*, **140**, 60 (2007).
8. M. I. Shariful, T. Sepehr, M. Mehrali, B. C. Ang and M. A. Amalina, *J. Appl. Polym. Sci.*, **135**, 45851 (2018).
9. Z. Xu, G. Gao, B. Pan, W. Zhang and L. Lv, *Water Res.*, **87**, 378 (2015).
10. I. Petrinic, J. Korenak, D. Povodnik and C. Hélix-Nielsen, *J. Clean. Prod.*, **101**, 292 (2015).
11. J. Altmann, A. S. Ruhl, F. Zietzschmann and M. Jekel, *Water Res.*, **55**, 185 (2014).
12. M. A. Shaker and H. M. albishri, *Chemosphere*, **111**, 587 (2014).
13. N. Li, F. Fu, J. Lu, Z. Ding, B. Tang and J. Pang, *Environ. Pollut.*, **220**, 1376 (2017).
14. L. Lv, N. Chen, C. Feng, J. Zhang and M. Li, *RSC Adv.*, **7**, 27992 (2017).
15. H.-C. Dang, X. Yuan, Q. Xiao, W.-X. Xiao, Y.-K. Luo, X.-L. Wang, F. Song and Y.-Z. Wang, *J. Environ. Chem. Eng.*, **5**, 4505 (2017).
16. N. M. Noor, R. Othman, N. M. Mubarak and E. C. Abdullah, *J. Taiwan Inst. Chem. Eng.*, **78**, 168 (2017).
17. W. Park, A. C. Gordon, S. Cho, X. Huang, K. R. Harris, A. C. Larson and D.-H. Kim, *ACS Appl. Mater. Inter.*, **9**, 13819 (2017).
18. N. Rodkate and M. Rutnakornpituk, *Carbohyd. Polym.*, **151**, 251 (2016).
19. X. Zhang, N. Zhang, C. Du, P. Guan, X. Gao, C. Wang, Y. Du, S. Ding and X. Hu, *Chem. Eng. J.*, **317**, 988 (2017).
20. Z. Hu, Q. Shao, M. G. Moloney, X. Xu, D. Zhang, J. Li, C. Zhang and Y. Huang, *Macromolecules*, **50**, 1422 (2017).
21. W. Zhu, W. Ma, C. Li, J. Pan and X. Dai, *Chem. Eng. J.*, **276**, 249 (2015).
22. J. Liu, H.-T. Wu, J.-f. Lu, X.-y. Wen, J. Kan and C.-h. Jin, *Chem. Eng. J.*, **262**, 803 (2015).
23. J. Xie, G. Zhong, C. Cai, C. Chen and X. Chen, *Talanta*, **169**, 98 (2017).
24. J. Huang, P. Su, L. Zhou and Y. Yang, *Colloids Surf., A*, **490**, 241 (2016).
25. P. Pingmuanglek, N. Jakrawatana and S. H. Gheewala, *J. Clean. Prod.*, **162**, 1075 (2017).
26. H. Jiang, Y. Qin, S. I. Gadow and Y.-Y. Li, *Int. J. Hydrogen Energy*, **42**, 2868 (2017).
27. H. Lu, C. Lv, M. Zhang, S. Liu, J. Liu and F. Lian, *Energy Convers. Manage.*, **132**, 251 (2017).
28. J. Cheng, J. Zhang, R. Lin, J. Liu, L. Zhang and K. Cen, *Bioresour. Technol.*, **228**, 348 (2017).
29. X. Xie, H. Xiong, Y. Zhang, Z. Tong, A. Liao and Z. Qin, *J. Environ. Chem. Eng.*, **5**, 2800 (2017).
30. A. R. Garcia, C. Lacko, C. Snyder, A. C. Bohórquez, C. E. Schmidt

and C. Rinaldi, *Colloids Surf. Physicochem. Eng. Aspects*, **529**, 119 (2017).
31. Z. Guo, J. Fan, J. Zhang, Y. Kang, H. Liu, L. Jiang and C. Zhang, *J. Taiwan Inst. Chem. Eng.*, **58**, 290 (2016).
32. A. Hajlane, H. Kaddami and R. Joffe, *Ind. Crop. Prod.*, **100**, 41 (2017).
33. D. Morillo Martín, M. Faccini, M. A. García and D. Amantia, *J. Environ. Chem. Eng.*, **6**, 236 (2018).
34. Q. Lin, J. Pan, Q. Lin and Q. Liu, *J. Hazard. Mater.*, **263**, 517 (2013).
35. L. Lu, J. Li, D. H. L. Ng, P. Yang, P. Song and M. Zuo, *J. Ind. Eng. Chem.*, **46**, 315 (2017).
36. W. Wang, T. Liang, H. Bai, W. Dong and X. Liu, *Carbohydr. Polym.*, **179**, 297 (2018).
37. T. Zhai, Q. Zheng, Z. Cai, H. Xia and S. Gong, *Carbohydr. Polym.*, **148**, 300 (2016).
38. L. Wang and D. E. Giammar, *J. Colloid Interface Sci.*, **448**, 331 (2015).
39. X. Liu, M. Liu and L. Zhang, *J. Colloid Interface Sci.*, **511**, 135 (2018).
40. D. Kołodyńska, J. Krukowska-Bąk, J. Kazmierczak-Razna and R. Pietrzak, *Micropor. Mesopor. Mater.*, **244**, 127 (2017).
41. N. A. Fakhre and B. M. Ibrahim, *J. Hazard. Mater.*, **343**, 324 (2018).
42. X. Ma, X. Liu, D. P. Anderson and P. R. Chang, *Food Chem.*, **181**, 133 (2015).
43. Q. Liu, F. Li, H. Lu, M. Li, J. Liu, S. Zhang, Q. Sun and L. Xiong, *Food Chem.*, **242**, 256 (2018).
44. N. Yin, K. Wang, Y. A. Xia and Z. Li, *Desalination*, **430**, 120 (2018).
45. T. Liu, X. Han, Y. Wang, L. Yan, B. Du, Q. Wei and D. Wei, *J. Colloid Interface Sci.*, **508**, 405 (2017).
46. Q. Yuan, Y. Chi, N. Yu, Y. Zhao, W. Yan, X. Li and B. Dong, *Mater. Res. Bull.*, **49**, 279 (2014).
47. H. L. Fan, S. F. Zhou, W. Z. Jiao, G. S. Qi and Y. Z. Liu, *Carbohyd. Polym.*, **174**, 1192 (2017).
48. Q. Hu, Z. Xiao, X. Xiong, G. Zhou and X. Guan, *J. Environ. Sci.*, **27**, 207 (2015).
49. J. N. Putro, S. P. Santoso, S. Ismadji and Y.-H. Ju, *Micropor. Mesopor. Mater.*, **246**, 166 (2017).
50. A. A. Yakout, R. H. El-Sokkary, M. A. Shreadah and O. G. Abdel Hamid, *Carbohyd. Polym.*, **172**, 20 (2017).
51. T. W. Cheng, M. L. Lee, M. S. Ko, T. H. Ueng and S. F. Yang, *Appl. Clay Sci.*, **56**, 90 (2012).

Supporting Information

Aminated cassava residue-based magnetic microspheres for Pb(II) adsorption from wastewater

Xinling Xie[*,], Jie Huang[*], Youquan Zhang[*,†], Zhangfa Tong[*], Anping Liao[***], Xingkui Guo[**,****], Zuzeng Qin[*,†], and Zhanhu Guo[**,†]**

*School of Chemistry and Chemical Engineering, Guangxi Key Laboratory of Petrochemical Resource Processing and Process Intensification Technology, Guangxi University, Nanning 530004, Guangxi, China
**Integrated Composites Laboratory (ICL), Department of Chemical and Biomolecular Engineering, University of Tennessee, Knoxville, Tennessee 37966, USA
***Key Laboratory of Chemical and Biological Transformation Process of Guangxi Higher Education Institutes, Guangxi University for Nationalities, Nanning 530006, Guangxi, China
****College of Chemical and Environmental Engineering, Shandong University of Science and Technology, Qingdao 266590, China
(*Received 20 July 2018 • accepted 14 November 2018*)

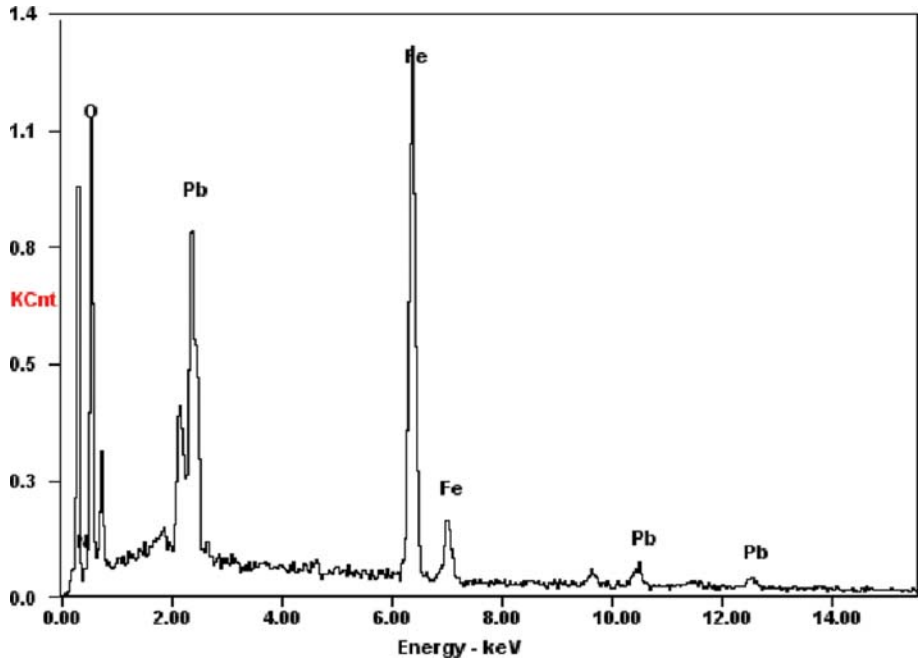

Fig. S1. EDAX of the ACRPM adsorbed the Pb (II).

Table S1. Texture properties of the ACRM and ACRPM

Samples	Specific surface area (m^2/g)	Pore volume (m^3/g)	Pore radius (nm)
ACRM	3.023	0.01222	26.65
ACRPM	12.34	0.05510	17.85